3-11-2019

Material and Regenerative Properties of an Osteon-Mimetic Cortical Bone-Like Scaffold

Danial Barati

Ozan Karaman

Seyedsina Moeinzadeh

Safaa Kader

Esmaiel Jabbari

Regenerative Biomaterials, 2019, 89–98
doi: 10.1093/rb/rbz008
Advance Access Publication Date: 11 March 2019
Research Article

Material and regenerative properties of an osteon-mimetic cortical bone-like scaffold

Danial Barati[1,†], Ozan Karaman [1,†,‡], Seyedsina Moeinzadeh[1], Safaa Kader[2] and Esmaiel Jabbari [1,*]

[1]Biomimetic Materials and Tissue Engineering Laboratory, Department of Chemical Engineering, University of South Carolina, Columbia, SC 29208, USA and [2]Department of Chemistry and Biochemistry, University of South Carolina, Columbia, SC 29208, USA

*Correspondence address. Department of Chemical Engineering, Swearingen Engineering Center, Rm 2C11, University of South Carolina, Columbia, SC 29208, USA. Tel: +803-777-8022; Fax: +803-777-0973; E-mail: jabbari@cec.sc.edu

[†]These authors contributed equally to this work.
[‡]Present address: Department of Biomedical Engineering, İzmir Katip Celebi University, İzmir 35620, Turkey.

Received 7 December 2018; revised 16 January 2019; accepted on 29 January 2019

Abstract

The objective of this work was to fabricate a rigid, resorbable and osteoconductive scaffold by mimicking the hierarchical structure of the cortical bone. Aligned peptide-functionalize nanofiber microsheets were generated with calcium phosphate (CaP) content similar to that of the natural cortical bone. Next, the CaP-rich fibrous microsheets were wrapped around a microneedle to form a laminated microtube mimicking the structure of an osteon. Then, a set of the osteon-mimetic microtubes were assembled around a solid rod and the assembly was annealed to fuse the microtubes and form a shell. Next, an array of circular microholes were drilled on the outer surface of the shell to generate a cortical bone-like scaffold with an interconnected network of Haversian- and Volkmann-like microcanals. The CaP content, porosity and density of the bone-mimetic microsheets were 240 wt%, 8% and 1.9 g/ml, respectively, which were close to that of natural cortical bone. The interconnected network of microcanals in the fused microtubes increased permeability of a model protein in the scaffold. The cortical scaffold induced osteogenesis and vasculogenesis in the absence of bone morphogenetic proteins upon seeding with human mesenchymal stem cells and endothelial colony-forming cells. The localized and timed-release of morphogenetic factors significantly increased the extent of osteogenic and vasculogenic differentiation of human mesenchymal stem cells and endothelial colony-forming cells in the cortical scaffold. The cortical bone-mimetic nature of the cellular construct provided balanced rigidity, resorption rate, osteoconductivity and nutrient diffusivity to support vascularization and osteogenesis.

Keywords: bone regeneration; cortical bone-like; osteon-mimetic; calcium phosphate nucleated nanofiber microsheet; vascularized osteogenesis

Introduction

There is a clinical need for tissue-engineered cellular constructs for reconstruction of large skeletal defects [1]. Approximately 1.5 million Americans every year suffer from bone loss that requires grafting to bridge the gap [2]. Patients with large traumatic skeletal injuries undergo multiple costly operations followed by rehabilitation mainly due to insufficient mechanical stability, lack of vascularity and inadequate resorption of the graft [3]. Autograft bone is the gold standard for reconstruction of bone defects [4]. However, there is insufficient source of autograft bone for patients with large skeletal defects [5]. The use of frozen or freeze-dried allogeneic bone increases the risk of transmission of unknown pathogens [6, 7]. To this end, the overall goal of this research was to engineer a bone-mimetic scaffold as a substitute for autograft in reconstruction of large bone defects.

The natural bone matrix with its interconnected network of microcanals and high apatite content provides mechanical stability, osteoconductivity and a dense vascular network for exchange of nutrients and oxygen [8–10]. Mechanical toughness of the cortical bone is rooted in its high quantity of calcium phosphate (CaP) nanocrystals deposited on aligned collagen fibrils [11, 12], which assemble to form microtubular osteons [13]. The adjacent osteons are connected in the transverse direction by Volkmann canals to uniformly supply the osseous tissue with nutrients and oxygen and remove waste [14]. The fusion of the microtubular osteons generates the rigid and tough shell of the cortical bone. We previously showed that nanofibers functionalized with CaP nucleating peptides served as a template for nucleation and growth of CaP nanocrystals [15]. We further discovered that organic acids like citric acid significantly increased CaP deposition on the fibers [16] to the extent found in the natural dense bone [17]. Further, we demonstrated that relaxation and shrinkage of the nanofibers upon annealing can be used for fusion and lamination of the microsheets [17].

Scaffold geometry, porosity, pore size and pore connectivity affect transport of nutrients, scaffold rigidity and degradation, and uniformity of bone formation [18, 19]. The ideal scaffold for regeneration of bone tissue should balance mechanical properties, nutrient permeability and scaffold resorption [20–22]. Many techniques such as freeze-drying, gas foaming, solvent casting/porogen leaching and 3D printing have been used to generate porous scaffolds [23–26]. However, the scaffolds fabricated using these techniques lack the rigidity, pore architecture and interconnectivity of the natural bone ECM. Therefore, there is a need to develop cellular scaffolds that mimic the natural tissue microstructure of dense, load-bearing cortical bone.

The objective of this work was to synthesize a rigid, resorbable and osteoconductive scaffold for implantation in large bone defects by mimicking the hierarchical structure of the cortical bone. The following approach was used to achieve the objective. CaP nanocrystals were grown on aligned nanofiber microsheets generated by electrospinning of a blend of high molecular weight (MW) poly(L-lactide) (PLA) and a conjugate of low MW poly(DL-lactide) (LMWPLA) with CaP-nucleating glutamic acid (GLU) peptide (LMWPLA-GLU). The CaP-nucleated microsheets were laminated around microneedles to form osteon-mimetic microtubes. A set of the microtubes were assembled around a solid rod and the assembly was annealed to fuse the microtubes and produce a cortical shell. Next, an array of circular microholes were drilled on the outer surface of the cortical shell to generate Volkmann-like microcanals in the perpendicular direction to the lumen of microtubes to generate a cortical bone-like scaffold. The scaffold was characterized with respect to CaP content, compressive modulus, porosity, permeability, resorption and the extent of osteogenesis and vasculogenesis with human mesenchymal stem cells (hMSCs), endothelial colony-forming cells (ECFCs) and nanogels (NGs) for timed-release of bone morphogenetic protein-2 (BMP2) and vascular endothelial growth factor (VEGF).

Materials and experiments

Materials

PLA with weight-average MW of 90 kDa was from LACTEL (Cupertino, CA). L-lactide (L) and glycolide (G) monomers were from Ortec (Easley, SC). Poly(ethylene glycol) (PEG, $\overline{M}_w$ = 8 and 12 kDa), porcine skin gelatin (type A, 300 bloom), human VEGF, *recombinant human* BMP2, their enzyme-linked immunosorbent assay (ELISA) kits, methacrylic anhydride (MA), acryloyl chloride (AC), ninhydrin reagent and Alizarin red stain were from Sigma–Aldrich (St. Louis, MO). 1,1,1,3,3,3-hexafluoro-2-propanol (HFIP) and citric acid (CA) were from VWR (West Chester, PA). The Irgacure 2959 photoinitiator was from CIBA (Tarrytown, NY). Bovine serum albumin (BSA) was from Jackson ImmunoResearch (West Grove, PA). Dulbecco's Modified Eagle's Medium (DMEM) was from Gibco BRL (Grand Island, NY). Full EGM-2 medium (BulletKit), ascorbic acid (AA), β-glycerophosphate (βGP), dexamethasone (DEX) were from Lonza (Allendale, NJ). PECAM-1 (CD31) and bovine anti-rabbit IgG-FITC (secondary antibody) were from Santa Cruz Biotechnology (Dallas, TX). Fetal bovine serum (FBS) was from Atlas Biologicals (Fort Collins, CO). The QuantiChrom calcium and alkaline phosphatase (ALP) assays were from Bioassay Systems (Hayward, CA). The Quant-it PicoGreen assay was from Invitrogen (Carlsbad, CA). Human MSCs and ECFCs were received from Lonza (Allendale, NJ) and Boston Children Hospital (Boston, MA), respectively.

Materials synthesis

Acrylate-terminated LMWPLA (Ac-LMWPLA) with MW of 5.3 kDa and polydispersity index (PI) of 1.2 was synthesized and characterized as we previously described [15, 27]. The amino acid sequence Glu-Glu-Gly-Gly-Cys hereafter denoted by GLU peptide was synthesized, conjugated to Ac-LMWPLA and the conjugate was characterized as we previously described [15]. The average number of peptides per GLU-LMWPLA conjugate was 1.3 [15]. PEG with short L and G segments (PEG-LG) was synthesized, functionalized with succinimide groups and purified as we previously described [28, 29]. Gelatin methacryloyl (GelMA) was synthesized as previously described [28].

Production of cortical bone-like scaffolds

Aligned nanofiber microsheets were generated by electrospinning of a solution of 8 wt% PLA and 1.5 wt% LMWPLA-GLU in HFIP as we previously described [15, 30]. The average thickness of the PLA/LMWPLA-GLU microsheets, hereafter denoted by NF, was 6 μm and the average diameter of the fibers was 200 ± 60 nm [15]. Next, the microsheets were incubated in a modified simulated body fluid (SBF) containing 6 mM citric acid for CaP nucleation and growth as we previously described [15, 16]. After CaP nucleation, the microsheet volume was determined from the measurements of its thickness and surface area. Apparent density was determined by dividing the microsheet mass by its volume. The volume porosity (Pv) of the microsheets was determined from the measurements of wet weight (Ww), wet volume (V_w) and dry weight as we previously described [31]. The degradation of microsheets was measured by incubation in SBF at 37°C as we previously described [15].

The following procedure was used to produce a cortical bone-like scaffold. A CaP nucleated microsheet (5 cm in length by 1 cm in width, Fig. 1a) was wrapped around a 21-gauge needle (0.81 mm outside diameter, Fig. 1b) to form a microtubular structure. The wrapped microsheet was annealed at 85°C for 10 min to fuse the laminated layers and produce an osteon-mimetic microtube. To produce a cortical bone scaffold, the CaP-nucleated microsheets were individually wrapped around needles between 10 and 30 times but unlike the previous procedure the microtube-needle assemblies were not annealed separately. Instead, a set of the microtube-needle assemblies were assembled around a stainless steel rod (Fig. 1c) and the bundle was placed inside an elastic rubber sleeve to firmly pack

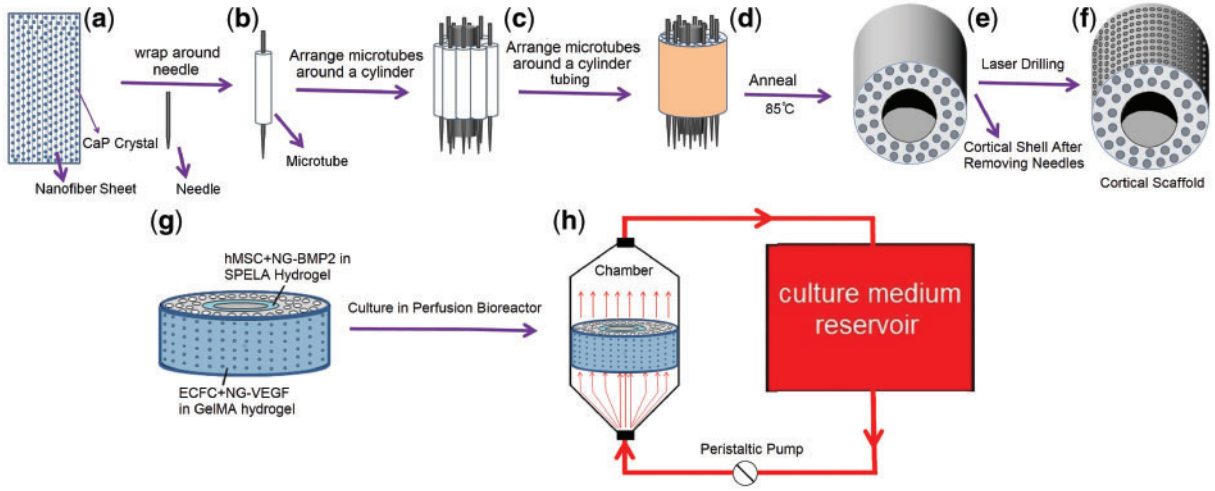

Figure 1. Schematic diagram for the production of a cortical bone-like scaffold. The CaP nucleated microsheets (**a**) were laminated around a needle to form an osteon-mimetic microtube (**b**). A set of the microtubes (**c**) were firmly assembled around a cylindrical rod by placing the bundle inside an elastic rubber sleeve (**d**) and annealed at 85°C to fuse the microtubes (**e**). An array of microholes were drilled on the outer surface of the fused microtubes, the rod and needles were removed to generate a cortical scaffold (**f**); the culture system consisting of a perfusion bioreactor containing the cell-seeded cortical scaffolds (**g**), a peristaltic pump, and a reservoir for oxygenation of the culture medium (**h**)

the microtubes around the rod (Fig. 1d). Next, the packed microtube-rod assembly was annealed at 85°C under vacuum for 45 min to fuse the microtubes. After cooling, the cylindrical rod and needles were removed to produce a nanostructured cortical bone-like scaffold with Haversian-like microcanals (Fig. 1e). Next, an array of circular microholes 1 mm apart was drilled on the outer surface of the cortical shell traversing the shell thickness to generate Volkmann-like microcanals perpendicular to the Haversian-like canals (Fig. 1f). The microholes were drilled with a scanning deep-ultraviolet laser micro-drilling system (Precision MicroFab, Curtis Bay, MD, USA). The array of Haversian- and Volkmann-like canals in the cortical-like scaffold formed an interconnected network of microcanals for cell migration, diffusion of nutrients and oxygen, and microvessel formation within the cortical scaffold. The calcium content, calcium to phosphate elemental ratio (Ca/P) and CaP content of the scaffolds were measured as we described previously [15, 32]. Mutilayer microsheets with 10 layers were used for the measurement of compressive modulus using a rheometer in a uniaxial compressive mode as we previously described [33].

Synthesis of BMP2- and VEGF-conjugated nanogels

BMP2 was conjugated to succinimide-terminated PEG-LG with PEG MW of 8 kDa, L to PEG molar ratio of 6.4, G to PEG ratio of 2 and overall PEG-LG MW of 10.3 kDa (hereafter referred to as P8I) as we previously described [28]. VEGF was conjugated to succinimide-terminated PEG-LG with PEG MW of 12 kDa, L to PEG ratio of 6.7, G to PEG ratio of 4.4 and overall PEG-LG MW of 15 kDa (hereafter referred to as P12II) as we previously described [28]. BMP2 and VEGF proteins were conjugated to succinimide-terminated PEG-LG macromer and the conjugates were assembled into nanogels as we previously described [34]. The amount of conjugated BMP2 or VEGF was measured by ELISA as we previously described [28]. The release kinetic of VEGF and BMP2 from P8I and P12II NGs, respectively, is shown in Supplementary Fig. S1. VEGF grafted to P12II NGs (VEGF-NGs) was released steadily in 10 days whereas BMP2 grafted to P8I NGs (BMP2-NGs) was released in 21 days [28].

Release characteristics of BSA from the cortical scaffold

Ten laminated microtubes were fused to form a hollow cylinder with inner diameter of 0.8 mm. The lumen of the fused microtubes, with or without micro-drilling, was filled with 100 mg/ml solution of BSA in PBS and both ends of the bundle were sealed to prevent leakage. Next, the BSA-loaded fused bundles were placed in a 2-ml centrifuge tube and incubated in 1 ml of PBS with orbital shaking. The amount of BSA in the supernatant was measured with the ninhydrin reagent as we previously described [15, 35].

Cell culture

Human MSCs were cultured in basal MSC medium as we previously described (passaged <5 times) [25]. Human ECFCs were cultured in full EGM-2 medium supplemented with 20% FBS on 1% gelatin-coated flasks as described previously (passaged <4 times) [36].

Culture of hMSCs on microsheets and microtubes

The surface of sterilized microsheets and microtubes was wetted by immersion in basal medium for 1 h prior to cell seeding. Each microsheet or microtube was injected with 5 ml of hMSC suspension (5×10^6 cells/ml) in basal medium resulting in a surface density of 1×10^5 cells/cm^2. After 24-h incubation, the medium was replaced with osteogenic medium (basal medium supplemented with 100 nM DEX, 50 μg/ml AA, 10 mM ßGP) and cultured for up to 28 days.

Culture of hMSCs and ECFCs in the cortical scaffolds

A perfusion cell culture system was used to culture hMSCs/ECFC-seeded cortical scaffolds. The cortical scaffolds were produced by fusion of 25 microtubes with 8 mm outer diameter, 2.5 mm shell thickness and 5 mm length. The lumina of the cortical scaffolds was injected with a suspension of hMSCs and BMP2-NGs in a SPELA gel precursor solution (Fig. 1g). The SPELA precursor solution

consisted of 200 mg SEPLA macromer, 4 mg Ac-GRGD cell adhesion peptide and 7.5 mg Irgacure-2959 photo-initiator in PBS. Next, hMSCs at a density of 5×10^6 cells/ml and 20 mg BMP2-NGs (1.2 μg BMP2) were suspended in 1 ml of sterile SPELA precursor solution. A 1.5-mm diameter needle (G-20) was placed in the center of the cortical scaffold and the resulting SPELA suspension was injected in the scaffold lumen. The injected precursor solution was crosslinked by UV irradiation as we previously described [33]. The channel left behind after removal of the needle directed the flow of culture medium through the cortical scaffold in the perfusion culture system. Then, ECFCs+MSCs (1:1 ratio) at a density of 5×10^6 cells/ml and 2 mg VEGF-NGs were added to the sterile GelMA precursor solution (50 mg GelMA and 7.5 mg photo-initiator in 1 ml PBS). The cortical scaffold was inserted inside a cylindrical Teflon mold with 10 mm inside diameter. Next, the volume between the cortical scaffold and Teflon mold was injected with the GelMA precursor solution. Then, the suspension was crosslinked by UV irradiation as we previously described [33] to form a thin layer of GelMA hydrogel (1 mm thickness) on the outer surface of the cortical scaffold (Fig. 1g). After removing the Teflon mold, the cell-seeded cortical scaffold was press-fitted into a silicone tube to yield the bioreactor section of the perfusion culture system (Fig. 1h). A medium reservoir for simultaneous perfusion of 32 cortical scaffolds was used to oxygenate the culture medium (Fig. 1h). The cell-seeded cortical scaffolds were perfused with a 50:50 mixture of vasculogenic and osteogenic medium (without VEGF, BMP2 or DEX) for the first 10 days followed by osteogenic medium (without DEX or BMP2) for the remaining 11 days.

Biochemical, mRNA, protein analysis and immunofluorescent staining

The cell-seeded samples were evaluated with respect to DNA content, ALP activity, calcium content, mRNA expression of osteogenic markers Runx2, osteocalcin (OC), and collagen type I (Col I), mRNA expression of vasculognic markers VE-cadherin, von Willebrand factor (vWF), and CD31, and protein expression of CD31 as we previously described [25]. The forward and reverse primers for the osteogenic and vasculogenic markers are provided in Supplementary Table S1 [28]. The mRNA fold difference in expression for the gene of interest was normalized against day 1 expression as we previously described [25]. The hMSC-seeded microsheets were immunofluorescent stained for OC and osteopontin (OP) as we previously described [15].

Statistical analysis

All experiments were done in triplicate. Significant differences between experimental groups were evaluated using a two-way ANOVA test with P-values < 0.05 as we previously described [25].

Results

Characterization of the microsheets, microtubes and cortical scaffolds

Figure 2a shows SEM image of the aligned nanofibers of a microsheet nucleated with 240 wt% CaP nanocrystals. The average size of the fibers in Fig. 2a was 80 nm and the microsheet thickness was 20 μm. The elemental spectrum of the mineralized microsheets, measured by energy-dispersive X-ray spectroscopy (EDS) as described previously [16], is shown in Supplementary Fig. S2. The images in Fig. 2b and c show the osteon-mimetic microtubes (240 wt% CaP) with wall thickness to outside radius of 0.7 and 0.35, respectively. Figure 2d shows a cortical scaffold with inner and outer diameters of 2 and 3.5 cm, respectively, produced from the fusion of 220 CaP-nucleated microtubes (240 wt% CaP, 300 μm inner diameter and 1 mm outer diameter). Figure 2e shows an array of microholes with diameter of 80 μm and center-to-center distance of 1 mm on the outer surface of the cortical scaffold after laser drilling. A higher magnification of the microholes is shown in Fig. 2f.

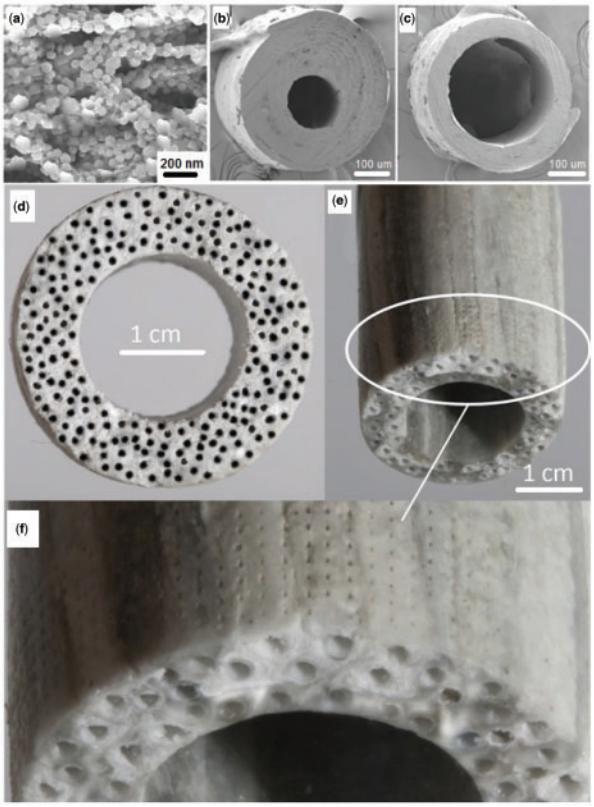

Figure 2. (**a**) A microsheet with 20 μm thickness composed of aligned nanofibers with average fiber diameter of 180 nm and 240 wt% CaP content; (**b**) cross-sectional image of a microtube with wall thickness to outside radius ratio of 0.7 and outside diameter of 350 μm; (**c**) cross-sectional image of a microtube with wall thickness to outside radius ratio of 0.35 and outside diameter of 350 μm); (**d**) Cross-sectional image of a cortical scaffold with inner and outer diameters of 2 and 3.5 cm, respectively, produced by fusion of 220 microtubes with inner and outer diameter of 300 μm and 1 mm, respectively; (**e**) Side-view of a cortical scaffold with inner and outer diameters of 1 and 2 cm, respectively, produced by fusion of 105 microtubes with inner and outer diameter of 300 μm and 1 mm, respectively; (**f**) Magnified side-view of the cortical scaffold in (e) showing the array of microholes drilled on the outer surface. The microholes which spanned the entire wall thickness were separated by 1 mm and their average diameter was 80 μm

The effect of incubation time of the microsheets in the modified SBF with or without the addition of citric acid on CaP nucleation on the nanofibers is shown in Fig. 3a. The addition of citric acid to the modified SBF significantly increased CaP content of the microsheets from 148 ± 20 wt% based on the fiber weight to 239 ± 30 wt% after 24-h incubation. Porosity of the microsheets decreased after annealing (Fig. 3b). Porosity of the pristine (without CaP) microsheets decreased from 80 ± 15% before annealing to 30 ± 3% after annealing whereas the porosity of those microsheets with 240 wt% CaP decreased from 42 ± 5% to 8 ± 2%. The porosity of the

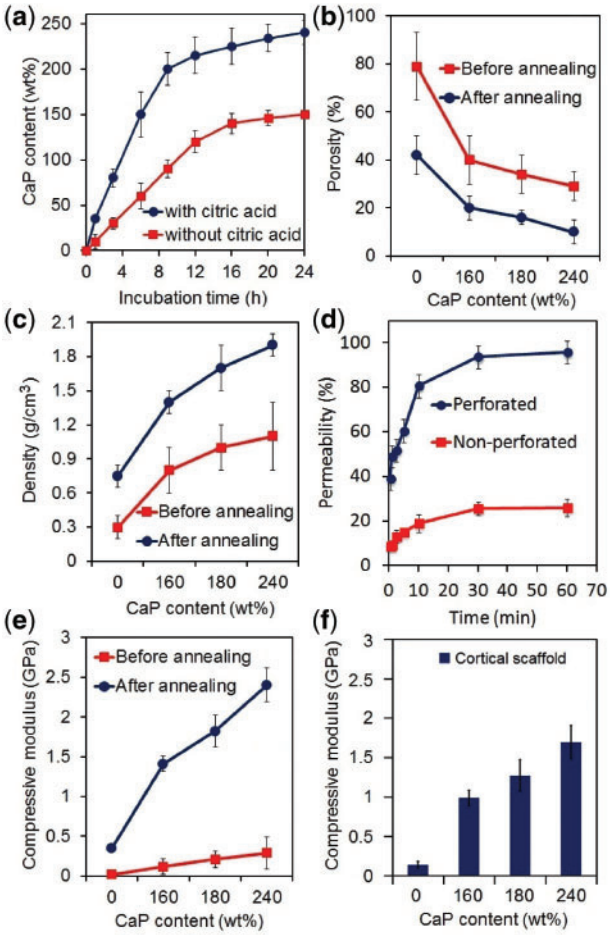

Figure 3. (**a**) the Effect of incubation time of the microsheets in the modified SBF with and without citric acid on CaP nucleation; The effect of CaP content on porosity (**b**) and density (**c**) of the microsheets before and after annealing; (**d**) the release profile of BSA from the fused microtubes before and after micro-drilling; (**e**) the effect of CaP content on the compressive modulus of the microsheets before and after annealing; (**f**) the effect of CaP content on the compressive modulus of the cortical scaffolds. There was a statistically significant difference between the CaP content, porosity, density, BSA release and compressive modulus of 'after annealing' and 'before annealing' groups

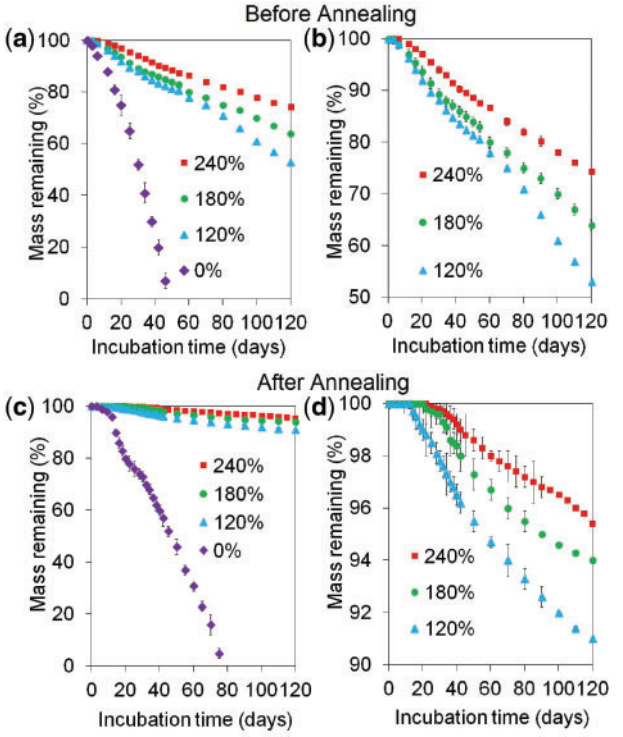

Figure 4. Mass loss of the cortical scaffolds with incubation time in SBF with 120, 180 and 240 wt% CaP content before (**a** and **b**) and after (**c** and **d**) annealing; figures (b) and (d) represent the magnified versions of figures (a) and (c), respectively. There was no difference in mass loss of the scaffolds with 240 and 180 wt% CaP as well as those with 120 and 180 wt% CaP. There was a significant difference between the mass loss of scaffolds with 240 and 120 wt% CaP. The mass loss of the scaffolds with 120, 180 and 240 wt% CaP was significantly lower than those with no CaP

annealed microsheets with 240 wt% CaP was close to that of the natural cortical bone at ~15% [37]. The density of microsheets with zero and 240 wt% CaP before annealing was 0.3 ± 0.1 and 1 ± 0.2 g/cm^3, respectively, which increased to 0.7 ± 0.1 and 1.9 ± 0.1 g/cm^3, after annealing (Fig. 3c). BSA was used to assess the permeability and interconnectivity of the cortical scaffold. The array of microholes drilled on the outer surface of the cortical scaffold increased the amount of BSA released from the lumen to the medium from 26 ± 3% before drilling to 96 ± 3% after drilling (Fig. 3d). The burst BSA release of ~40% after 1 min incubation was related to pore interconnectivity of the cortical scaffold as reported previously [38]. Compressive modulus of the mineralized microsheets increased by 10-fold after annealing due to relaxation and densification of the fibers (Fig. 3e). Compressive modulus of the microsheets with 240 wt% CaP content before annealing was 0.25 ± 0.15 MPa which increased to 2.5 ± 0.4 MPa after annealing. Compressive modulus of the cortical scaffolds increased from 0.15 ± 0.02 to 0.98 ± 0.12, 1.27 ± 0.21 and 1.76 ± 0.29 GPa when the CaP content increased from 0 to 160, 180 and 240 wt%, respectively (Fig. 3f). Compressive modulus of the scaffold with 240 wt% CaP was close to the reported modulus of natural human cortical bone at ~5GPa [39].

Degradation of the mineralized microsheets and cortical scaffolds

Mass loss of the CaP-nucleated microsheets with incubation in SBF at 37°C before and after annealing is shown in Fig. 4a and c, respectively. The magnified version of Fig. 4a and c are shown in Fig. 4b and d, respectively. For a given time point, mass loss of the CaP-nucleated microsheets was significantly lower than the pristine microsheets regardless of annealing. The pristine microsheets without annealing completely degraded in 35 days whereas those after annealing degraded in 80 days. The mass remaining for CaP-nucleated microsheets without annealing after 120 days incubation ranged from 50 to 80 wt% compared with 90–98 wt% for those with annealing. CaP nucleation increased stability of the microsheets in SBF with or without annealing, as shown in the magnified Fig. 4b and d. Further, for a given CaP content and incubation time, annealed microsheets showed higher stability in SBF compared with those without annealing. In that regard, the mass remaining for the microsheets with 240 wt% CaP after 120 days incubation was 75 ± 5 wt% without annealing and 96 ± 3 wt% with annealing.

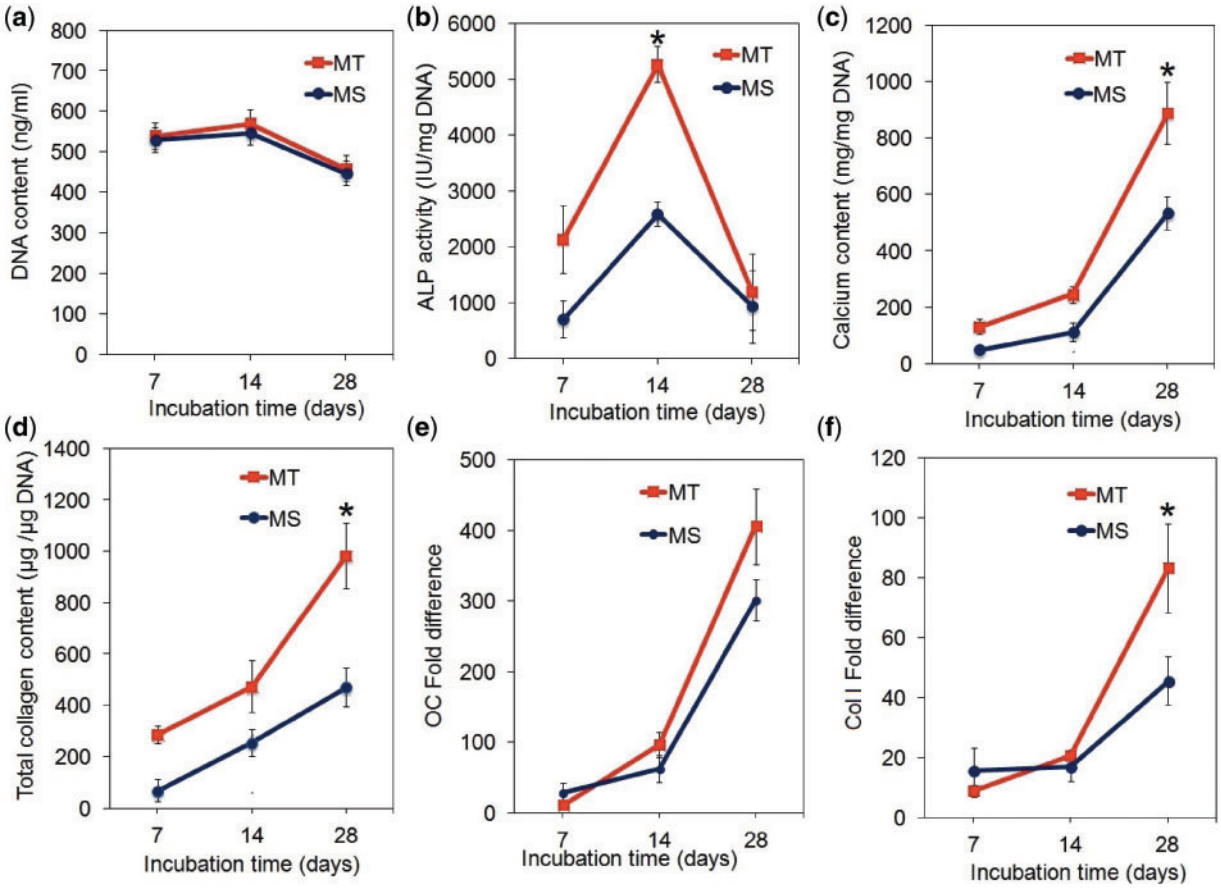

Figure 5. DNA Content (**a**), ALP activity (**b**), calcium content (**c**), total collagen content (**d**), fold difference in mRNA expression of OC (**e**) and Col I (**f**) of hMSCs seeded on the microsheets (MS, blue) or the microtubes (MT, red) and cultured in osteogenic medium for 28 days. The microsheets had a thickness of 20 µm and composed of nanofibers with diameter of 180 nm nucleated with 240 wt% CaP. The microtubes had inside and outside diameters of 0.8 and 1.2 nm, respectively, and nucleated with 240 wt% CaP. One star in the figures indicates a statistically significant difference ($P < 0.05$) between the two groups at a given time point. Error bars correspond to means ± 1 SD for $n = 3$

Osteogenic differentiation of hMSCs on the microsheets and microtubes

Human mesenchymal stem cells were seeded on the microsheets (MS) or in the lumen of the microtubes (MT) and cultured in osteogenic medium for 28 days. After a slight initial increase, DNA content of the samples decreased with osteogenic differentiation of hMSCs (Fig. 5a). DNA content (Fig. 5a) and peak ALP activity (Fig. 5b) of hMSCs seeded on the microsheets were different from those seeded on the microtubes. The peak ALP activity of hMSCs on the microsheets was 2580 ± 130 IU/mg DNA after 14 days as compared with 5270 ± 680 IU/mg DNA on the microtubes. The extent of mineralization and collagen content of hMSCs seeded on the microsheets and microtubes increased steadily with incubation from day 7–28 (Fig. 5c and d). The calcium content of hMSCs on the microtubes at 630 ± 40 mg/mg DNA after 28 days was higher than the microsheets at 450 ± 60 mg/mg DNA (Fig. 5c). The collagen content of the microtubes at 980 ± 130 µg/µg DNA after 28 days was higher than the microsheets at 470 ± 70 µg/µg DNA (Fig. 5d). Osteocalcin (OC, Fig. 5e) and Col I (Fig. 5f) mRNA expressions of hMSCs on the microsheets and microtubes increased steadily with incubation time. Col I expression of hMSCs in the microtubes was higher than those on microsheets (Fig. 5f). Immunofluorescent images of hMSC-seeded microsheets after 28 days incubation in osteogenic medium stained for OC and osteopontin (OP) are shown in Supplementary Fig. S3.

Co-culture of hMSCs and ECFCs in the cortical scaffolds

DNA content, ALP activity, calcium content and mRNA expression of osteogenic markers for the cortical scaffolds are shown in Fig. 6a–f. Groups included cortical scaffolds with cells and with growth factors in static culture (G1, blue curve), scaffolds with cells but without growth factors in perfusion culture (G2, light blue curve) and scaffolds with cells and with growth factors in perfusion culture as the experimental group (G3, red). DNA content of all groups decreased with incubation which was attributed to cell differentiation as we previously reported (Fig. 6a) [28]. ALP activity of all groups increased and peaked on day 14 and then decreased with incubation time (Fig. 6b). The peak ALP activity of G1, G2, G3 groups was 4250 ± 300, 3000 ± 100 and 6140 ± 200 IU/mg DNA, respectively. Interestingly, the cortical scaffolds with cells and with growth factors cultured in static mode (G1) had higher ALP activity (as well as higher Runx2 expression in Fig. 6d) than the scaffolds with cells but without growth factors cultured in perfusion mode (G2). Calcium content of all groups, as a measure of the extent of mineralization, steadily increased with incubation time (Fig. 6c). The calcium content of G3 group at 1120 ± 80 mg/mg DNA was higher than G1 and G2 groups at 1040 ± 60 and 720 ± 80 mg/mg

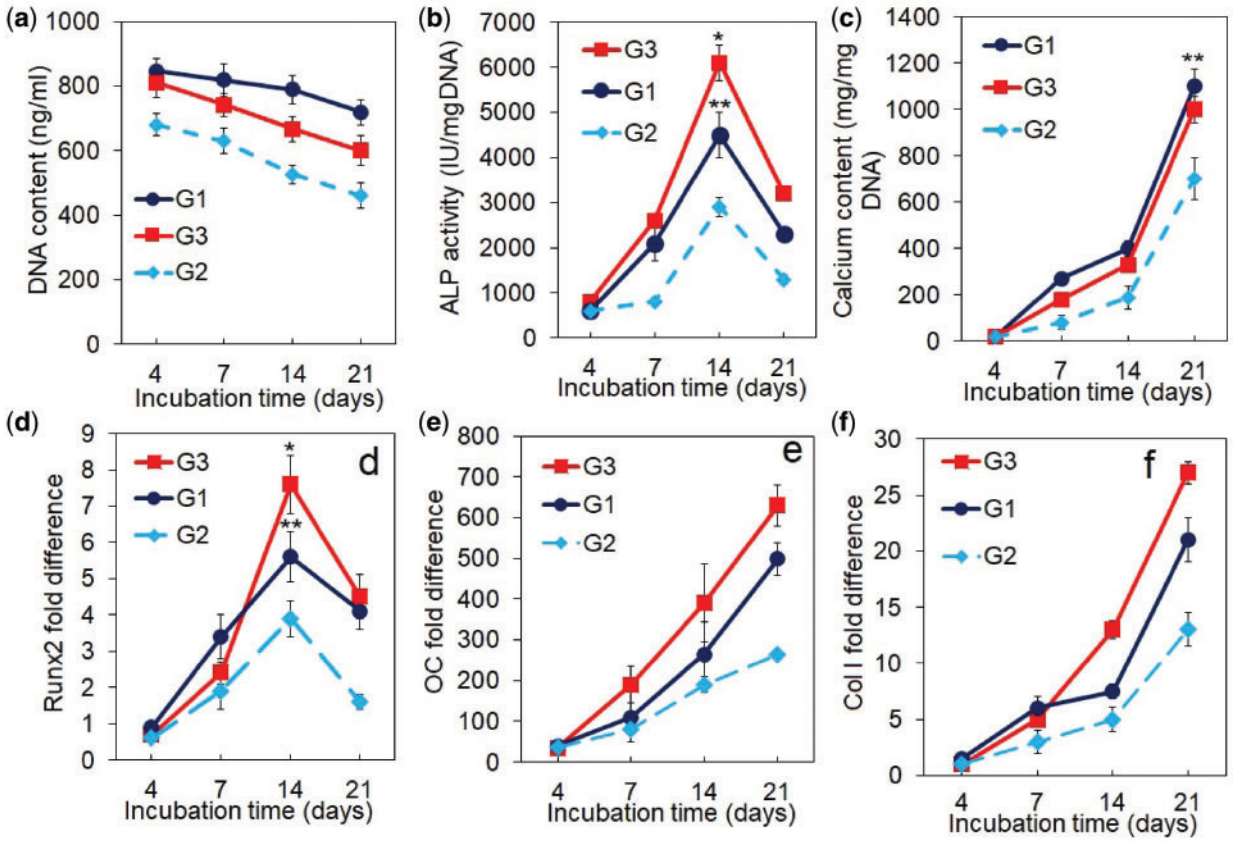

Figure 6. DNA Content (**a**), ALP activity (**b**), calcium content (**c**), mRNA expression level of osteogenic markers Runx2 (**d**), OC (**e**) and Col I (**f**) for the cortical scaffolds with hMSC/BMP2-NGs in the lumen and MSC+EFCF/VEGF-NGs on the outer surface and cultured in the perfusion bioreactor. Groups included cortical scaffolds with cells and with growth factors in static culture (G1, blue curve), scaffolds with cells but without growth factors in perfusion culture (G2, light blue curve), and scaffolds with cells and with growth factors in perfusion culture as the experimental group (G3, red). A star in the figures indicates a statistically significant difference between G3 and other groups. Error bars correspond to means ± 1 SD for $n = 3$

DNA, respectively. The mRNA expression of Runx2 transcription factor initially increased with incubation time for all groups, peaked at day 14 and then decreased (Fig. 6d). The OC and Col I mRNA expression of all groups increased steadily with incubation time (Fig. 6e and f). The cortical scaffolds with cells and growth factors in a perfusion culture (G3) had highest Runx2, OC and Col I expressions among all groups after 21 days of incubation.

The mRNA expression of vasculogenic markers VE-cadherin, vWF, and CD31, and CD31 protein expression for the cortical scaffolds are shown in Fig. 7a–e. The mRNA expression of VE-cadherin, vWF and CD31 of all groups increased with incubation time (Fig. 7a–c). The cortical scaffolds with cells and growth factors in perfusion culture (G3) had highest expression of vasculogenic markers among all groups. CD31 protein expression of all groups (Fig. 7d and e) increased with incubation time consistent with the mRNA expression of vasculogenic markers (Fig. 7a–c). The CD31 protein expression of G3 group was highest among all groups. For example, after 10 days incubation, the normalized CD31 protein expression of G1, G2 and G3 groups was 0.4 ± 0.06, 0.32 ± 0.08 and 0.68 ± 0.12, respectively.

Discussion

The pore connectivity and architecture affect uniformity of nutrient and oxygen distribution in the scaffold [40, 41] as it was previously shown that anisotropic microcanals in tissue scaffolds improved bone ingrowth *in vitro* and *in vivo* [42]. Open and interconnected network of pores was shown to be essential for homogeneous vascularization [43, 44] and served as a guide for cell migration and bone formation in the central part of the scaffold [45]. It was demonstrated in a previous study that interconnected microcanals improved the flow of medium, nutrient transport and cell seeding efficiency in multilayer scaffolds [46]. Further, scaffolds with interconnected pores enhanced stability of the implant through mechanical interlocking between the scaffold and surrounding tissue [8]. In this work, we successfully used fusion of laminated microtubes and laser micro-drilling to generate CaP-rich, cortical-like scaffolds with interconnected microcanals in the axial and transverse directions.

Previous studies have shown a close correlation between the rate of scaffold resorption and bone formation [33, 47]. Porous ceramic scaffolds that displayed a progressive resorption concurrent with new bone deposition showed improved bone healing upon implantation in a critical-size sheep tibial defect [47]. Based on previous reports, it takes ~12 weeks for a newly formed callus to become load-bearing as patients undergoing alveolar bone reconstruction have to wait a minimum of 12 weeks for the formation of load-bearing bone on the regenerating membrane prior to implantation [48, 49]. Further, the implanted scaffold should resorb with time and transfer load to the newly formed tissue to reduce stress-shielding [50]. The results in Fig. 4 show that resorptions of <5% in

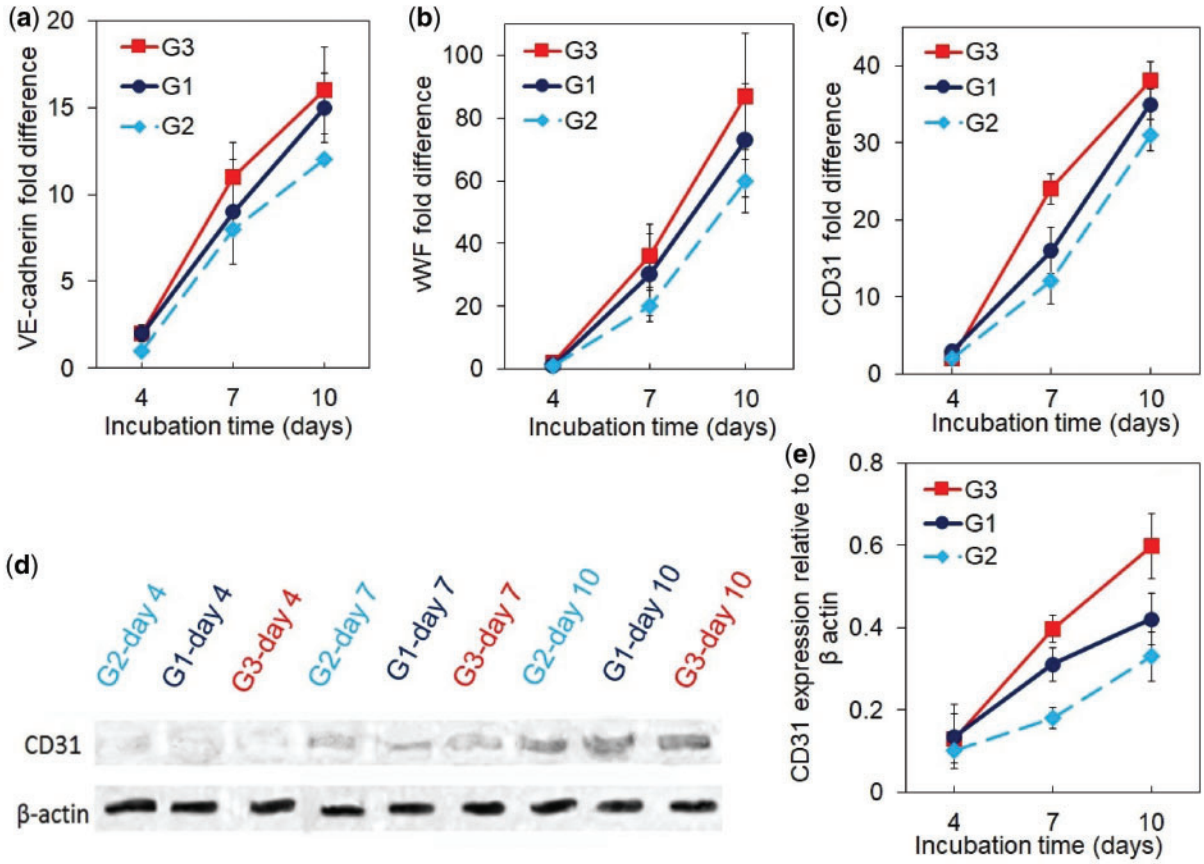

Figure 7. The mRNA expression level of vasculogenic markers VE-cadherin (**a**), vWF (**b**) and CD31 (**c**), Western-blot bands (**d**) and expression level (**e**) of CD31 protein for the cortical scaffolds with hMSC/BMP2-NGs in the lumen and MSC+EFCF/VEGF-NGs on the outer surface and cultured in the perfusion bioreactor. Groups included cortical scaffolds with cells and with growth factors in static culture (G1, blue curve), scaffolds with cells but without growth factors in perfusion culture (G2, light blue curve), and scaffolds with cells and with growth factors in perfusion culture as the experimental group (G3, red). A star in the figures indicates a statistically significant difference between G3 and other groups. Error bars correspond to means ± 1 SD for $n=3$

the first 12 weeks (load-bearing for 12 weeks) can be achieved with CaP-rich cortical scaffolds whereas the CaP-deficient scaffolds completely degraded in 12 weeks. For example, the cortical scaffolds with 120, 180 and 240 wt% CaP lost <8%, <6% and <4% of their initial weight, respectively, after 12 weeks of incubation in physiological medium (Fig. 4).

We previously showed that hMSC+ECFC/VEGF-NG seeded microchannels within a matrix seeded with hMSC/BMP2-NGs increased osteogenic and vasculogenic differentiation of the seeded cells [28]. We further showed that localized and timed-release of BMP2 and VEGF induced the production of paracrine signaling factors like basic fibroblast growth factor (bFGF), platelet-derived growth factor (PDGF) and transforming growth factor-β (TGF-β) by the cells, which led to the coupling of osteogenesis and vasculogenesis [28]. The results in Figs 6 and 7 show that hMSC/ECFC seeded cortical scaffolds differentiated and expressed markers of osteogenesis and vasculogenesis even in the absence of BMP2 and VEGF (see light blue curves in Figs 6 and 7). This was attributed to high CaP content of the cortical scaffolds and paracrine signaling between hMSCs and ECFCs enabled by the interconnected network of microcanals. As reported previously, CaP-rich matrices induce osteogenic differentiation of hMSCs through phosphate-ATP-adenosine metabolic signaling [51]. Further, the extent of osteogenic and vasculogenic differentiation of hMSCs and ECFCs in the cortical scaffolds significantly increased with the addition of BMP2-NGs and VEGF-NGs (compare red and light blue curves in Figs 6 and 7). Furthermore, the extent of osteogenic and vasculogenic differentiation of hMSCs and ECFCs in the cortical scaffolds in perfusion culture was slightly higher than those in static culture. Therefore, cell differentiation and matrix deposition was somewhat limited by nutrients and oxygen transport in the cortical scaffold in the static culture.

Conclusions

In this work, CaP-nucleated, aligned nanofiber microsheets were laminated around microneedles to form osteon-mimetic microtubes. The microtubes were assembled around a solid rod and annealed to form a cortical-like structure. The cortical-like structure was laser-drilled with an array of microholes to form a cortical bone-like scaffold with an interconnected network of Haversian- and Volkmann-like microcanals. CaP content of the cortical scaffolds reached 240% by weight of fibers which was close to that of the natural cortical bone. The high CaP content of the microsheets prolonged degradation of the cortical scaffolds which improved their long-term stability. The microtubular structure and interconnected network of microcanals increased transport of growth factors and nutrients in the cortical scaffold. hMSC encapsulated SPELA

hydrogel in the lumen of the cortical scaffolds and ECFC+hMSC encapsulated GelMA on the outer surface of the scaffolds stimulated osteogenesis and vasculogenesis in perfusion culture in the absence of morphogenetic factors. This was attributed to high CaP content of the cortical scaffolds and paracrine signaling between hMSCs and ECFCs via interconnected network of the scaffold's microcanals.

Supplementary data

Supplementary data are available at *REGBIO* online.

Acknowledgements

The content is solely the responsibility of the authors and does not necessarily represent the official views of the National Institutes of Health. The authors thank Dr Juan M. Melero-Martin (Department of Cardiac Surgery, Children's Hospital of Boston) for providing the endothelial colony forming cells. The authors thank Mr Joshua D. Walters for assistance in fabrication of the cortical scaffolds.

Funding

This work was supported by research grants to E. Jabbari from the National Science Foundation under Award Numbers CBET1403545 and IIP150024 and the National Institute of Arthritis and Musculoskeletal and Skin Diseases of the National Institutes of Health under Award Number AR063745.

Conflict of interest statement. None declared.

References

1. Cross JD, Ficke JR, Hsu JR *et al*. Battlefield orthopaedic injuries cause the majority of long-term disabilities. *J Am Acad Orthop Surg* 2011;**19**:S1–7.
2. Jahangir AA, Nunley RM, Mehta S *et al*. Bone-graft substitutes in orthopaedic surgery. *AAOS Now* 2008;**2**:35–7.
3. Bone Health and Osteoporosis: A Report of the Surgeon General. US Department of Health and Human Services 2004;**87**:1.
4. Ozdemir MT, Kir MC. Repair of long bone defects with demineralized bone matrix and autogenous bone composite. *Indian J Orthop* 2011;**45**:226.
5. Arrington ED, Smith WJ, Chambers HG *et al*. Complications of iliac crest bone graft harvesting. *Clin Orthop Relat Res* 1996;**329**:300–9.
6. Delloye C, Cornu O, Druez V *et al*. Bone allografts. *Bone Joint J* 2007;**89**:574–80.
7. Ng VY. Risk of disease transmission with bone allograft. *Orthopedics* 2012;**35**:679–81.
8. Karageorgiou V, Kaplan D. Porosity of 3D biomaterial scaffolds and osteogenesis. *Biomaterials* 2005;**26**:5474–91.
9. Salgado AJ, Coutinho OP, Reis RL. Bone tissue engineering: state of the art and future trends. *Macromol Biosci* 2004;**4**:743–65.
10. Adachi T, Osako Y, Tanaka M *et al*. Framework for optimal design of porous scaffold microstructure by computational simulation of bone regeneration. *Biomaterials* 2006;**27**:3964–72.
11. Xie B, Nancollas GH. How to control the size and morphology of apatite nanocrystals in bone. *Proc Natl Acad Sci U S A* 2010;**107**:22369–70.
12. Wang Q, Wang XM, Tian LL *et al*. In situ remineralizaiton of partially demineralized human dentine mediated by a biomimetic non-collagen peptide. *Soft Matter* 2011;**7**:9673–80.
13. Buckwalter JA, Glimcher MJ, Cooper RR *et al*. Bone biology. I: structure, blood supply, cells, matrix, and mineralization. *Instr Course Lect* 1996;**45**:371.
14. van Oers RFM, Ruimerman R, van Rietbergen B *et al*. Relating osteon diameter to strain. *Bone* 2008;**43**:476–82.
15. Karaman O, Kumar A, Moeinzadeh S *et al*. Effect of surface modification of nanofibres with glutamic acid peptide on calcium phosphate nucleation and osteogenic differentiation of marrow stromal cells. *J Tissue Eng Regen Med* 2016;**10**:E132–46.
16. Barati D, Walters JD, Pajoum Shariati SR *et al*. Effect of organic acids on calcium phosphate nucleation and osteogenic differentiation of human mesenchymal stem cells on peptide functionalized nanofibers. *Langmuir* 2015;**31**:5130–40.
17. Li B, Aspden RM. Composition and mechanical properties of cancellous bone from the femoral head of patients with osteoporosis or osteoarthritis. *J Bone Miner Res* 1997;**12**:641–51.
18. Smith LA, Liu X, Hu J *et al*. The influence of three-dimensional nanofibrous scaffolds on the osteogenic differentiation of embryonic stem cells. *Biomaterials* 2009;**30**:2516–22.
19. Deville S, Saiz E, Tomsia AP. Freeze casting of hydroxyapatite scaffolds for bone tissue engineering. *Biomaterials* 2006;**27**:5480–9.
20. Nerurkar NL, Elliott DM, Mauck RL. Mechanics of oriented electrospun nanofibrous scaffolds for annulus fibrosus tissue engineering. *J Orthop Res* 2007;**25**:1018–28.
21. Pham QP, Sharma U, Mikos AG. Electrospinning of polymeric nanofibers for tissue engineering applications: a review. *Tissue Eng* 2006;**12**:1197–211.
22. Richardson SM, Curran JM, Chen R *et al*. The differentiation of bone marrow mesenchymal stem cells into chondrocyte-like cells on poly-L-lactic acid (PLLA) scaffolds. *Biomaterials* 2006;**27**:4069–78.
23. Hutmacher DW. Scaffolds in tissue engineering bone and cartilage. *Biomaterials* 2000;**21**:2529–43.
24. Yoshimoto H, Shin YM, Terai H *et al*. A biodegradable nanofiber scaffold by electrospinning and its potential for bone tissue engineering. *Biomaterials* 2003;**24**:2077–82.
25. Moeinzadeh S, Barati D, Sarvestani SK *et al*. Experimental and computational investigation of the effect of hydrophobicity on aggregation and osteoinductive potential of BMP-2-derived peptide in a hydrogel matrix. *Tissue Eng A* 2015;**21**:134–46.
26. Lenhert S, Meier M-B, Meyer U *et al*. Osteoblast alignment, elongation and migration on grooved polystyrene surfaces patterned by Langmuir-Blodgett lithography. *Biomaterials* 2005;**26**:563–70.
27. Moeinzadeh S, Barati D, He X *et al*. Gelation characteristics and osteogenic differentiation of stromal cells in inert hydrolytically degradable micellar polyethylene glycol hydrogels. *Biomacromolecules* 2012;**13**:2073–86.
28. Barati D, Shariati SRP, Moeinzadeh S *et al*. Spatiotemporal release of BMP-2 and VEGF enhances osteogenic and vasculogenic differentiation of human mesenchymal stem cells and endothelial colony-forming cells co-encapsulated in a patterned hydrogel. *J Control Release* 2016;**223**:126–36.
29. Mercado AE, Jabbari E. Effect of encapsulation or grafting on release kinetics of recombinant human bone morphogenetic protein-2 from self-assembled poly(lactide-co-glycolide ethylene oxide fumarate) nanoparticles. *Microsc Res Tech* 2010;**73**:824–33.
30. Ma J, He X, Jabbari E. Osteogenic differentiation of marrow stromal cells on random and aligned electrospun poly(l-lactide) nanofibers. *Ann Biomed Eng* 2011;**39**:14–25.
31. Unosson JE, Persson C, Engqvist H. An evaluation of methods to determine the porosity of calcium phosphate cements. *J Biomed Mater Res B Appl Biomater* 2015;**103**:62–71.
32. Kourkoumelis N, Balatsoukas I, Tzaphlidou M. Ca/P concentration ratio at different sites of normal and osteoporotic rabbit bones evaluated by Auger and energy dispersive X-ray spectroscopy. *J Biol Phys* 2012;**38**:279–91.
33. Barati D, Moeinzadeh S, Karaman O *et al*. Time dependence of material properties of polyethylene glycol hydrogels chain extended with short hydroxy acid segments. *Polymer* 2014;**55**:3894–904.
34. Mercado AE, He X, Xu W *et al*. The release characteristics of a model protein from self-assembled succinimide-terminated poly(lactide-co-glycolide ethylene oxide fumarate) nanoparticles. *Nanotechnology* 2008;**19**:325609.
35. He X, Jabbari E. Solid-phase synthesis of reactive peptide crosslinker by selective deprotection. *Protein Pept Lett* 2006;**13**:715–8.
36. Melero-Martin JM, Khan ZA, Picard A *et al*. In vivo vasculogenic potential of human blood-derived endothelial progenitor cells. *Blood* 2007;**109**:4761–8.

37. Malo MKH, Rohrbach D, Isaksson H *et al*. Longitudinal elastic properties and porosity of cortical bone tissue vary with age in human proximal femur. *Bone* 2013;**53**:451–8.
38. Panyam J, Dali MM, Sahoo SK *et al*. Polymer degradation and in vitro release of a model protein from poly (D, L-lactide-co-glycolide) nano-and microparticles. *J Control Release* 2003;**92**:173–87.
39. Rho JY, Ashman RB, Turner CH. Young's modulus of trabecular and cortical bone material: ultrasonic and microtensile measurements. *J Biomech* 1993;**26**:111–9.
40. Choi S-W, Zhang Y, Xia Y. Three-dimensional scaffolds for tissue engineering: the importance of uniformity in pore size and structure. *Langmuir* 2010;**26**:19001–6.
41. Guarino V, Urciuolo F, Alvarez-Perez MA *et al*. Osteogenic differentiation and mineralization in fibre-reinforced tubular scaffolds: theoretical study and experimental evidences. *J R Soc Interface* 2012;**9**:2201–12.
42. Silva M, Cyster LA, Barry JJA *et al*. The effect of anisotropic architecture on cell and tissue infiltration into tissue engineering scaffolds. *Biomaterials* 2006;**27**:5909–17.
43. Hollister SJ. Porous scaffold design for tissue engineering. *Nat Mater* 2005;**4**:518–24.
44. Salerno A, Di Maio E, Iannace S *et al*. Tailoring the pore structure of PCL scaffolds for tissue engineering prepared via gas foaming of multi-phase blends. *J Porous Mater* 2012;**19**:181–8.
45. Chevalier E, Chulia D, Pouget C *et al*. Fabrication of porous substrates: a review of processes using pore forming agents in the biomaterial field. *J Pharm Sci* 2008;**97**:1135–54.
46. Papenburg BJ, Liu J, Higuera GA *et al*. Development and analysis of multi-layer scaffolds for tissue engineering. *Biomaterials* 2009;**30**:6228–39.
47. Mastrogiacomo M, Papadimitropoulos A, Cedola A *et al*. Engineering of bone using bone marrow stromal cells and a silicon-stabilized tricalcium phosphate bioceramic: evidence for a coupling between bone formation and scaffold resorption. *Biomaterials* 2007;**28**:1376–84.
48. Miyazaki T, Kim H-M, Kokubo T *et al*. Mechanism of bonelike apatite formation on bioactive tantalum metal in a simulated body fluid. *Biomaterials* 2002;**23**:827–32.
49. Gaggl A, Rainer H, Chiari FM. Horizontal distraction of the anterior maxilla in combination with bilateral sinuslift operation: preliminary report. *Int J Oral Maxillofac Surg* 2005;**34**:37–44.
50. Fischgrund J, Paley D, Suter C. Variables affecting time to bone healing during limb lengthening. *Clin Orthop Relat Res* 1994;**301**:31–7.
51. Shih YRV, Hwang Y, Phadke A *et al*. Calcium phosphate-bearing matrices induce osteogenic differentiation of stem cells through adenosine signaling. *Proc Natl Acad Sci U S A* 2014;**111**:990–5.